

Award Accounts

The Chemical Society of Japan Award for 2011

Development of Ultrafast Spectroscopy and Reaction Mechanisms Studied by the Observation of Ultrashort-Life Species and Transition States

Takayoshi Kobayashi[1,2,3,4]

[1]Advanced Ultrafast Laser Research Center, The University of Electro-Communications, 1-5-1 Chofugaoka, Chofu, Tokyo 182-8585

[2]JST, CREST, 5 Sanbancho, Chiyoda-ku, Tokyo 102-0075

[3]Department of Electrophysics, National Chiao Tung University, Hsinchu 30010, Taiwan

[4]Institute of Laser Engineering, Osaka University, 2-6 Yamada-oka, Suita, Osaka 565-0871

Received September 12, 2012; E-mail: kobayashi@ils.uec.ac.jp

1. Introduction

To gain a complete understanding of a chemical reaction it is necessary to determine the structural changes that occur to the reacting molecules during the reaction. Chemists have long dreamed of being able to determine the molecular structure changes that occur during a chemical reaction, including the structures of transition states (TSs). Using ultrafast spectroscopy to gain a detailed understanding of chemical reactions (including their TSs) promises to be a revolutionary way to increase reaction efficiencies and enhance the reaction products. These are difficult to do using conventional methods that are usually based on trial and error. To confirm the molecular structures of TSs predicted by theoretical analysis, chemists have long desired to directly observe the TSs of chemical reactions. Direct observations have been realized by ultrafast spectroscopy using ultrashort laser pulses. Our group has been able to stably generate visible to near-infrared sub-5-fs laser pulses using a noncollinear optical parametric amplifier (NOPA). We used these sub-5-fs pulses to study reaction processes (including their TSs) by detecting structural changes. We determine reaction mechanisms by observing the TSs in a chemical reaction and by performing density-functional theory calculations. In this paper photoisomerization in bacteriorhodopsin is described as an example of chemical reaction. Based on the results of the present study, it is concluded that the first process in the photophysical dynamics in bR is the deformation of the retinal configuration which decays within 30 fs near the C=N bond in the protonated Schiff base. It is followed by C=C stretching and then torsional motion of several periods around the C_{13}=C_{14} bond. This mode is as short as 30 fs, which corresponds to only 1.5 times the oscillation period (20 fs). This means that electronic redistribution, which occurs immediately after excitation (<2 fs), triggers rapid oscillation of C=N stretching. After a few oscillations, the energy is transferred to C=C stretching.

2. Femtosecond Pump Probe Experimental Setup Using Noncollinear Optical Parametric Amplification (NOPA)

2.1 Basics of Ultrashort Pulse Generation by Noncollinear Parametric Amplifier. In the following is a detailed description of the basic physics and technologies needed for the generation of ultrashort visible pulses which provide a powerful light source for time-resolved spectroscopy.

Optical parametric conversion has drawn great attention from scientists in the last decade since tunable broad band ultrafast laser pulses in ultraviolet (UV),[1] visible and near-infrared (NIR)[2–27] regions can be generated. It has grown to wide application especially in ultrafast time-resolved spectroscopy.

Utilizing the second-order nonlinear polarization effect in nonlinear crystals, optical parametric amplification (OPA) has been realized. The energy conversion from intense pump light (ω_p) to weak signal (ω_s) takes place and an idler $\omega_i = \omega_p - \omega_s$ is simultaneously generated through the second-order nonlinear polarization. Generated idler from vacuum continues to be coupled with pumping and amplifies the signal with the frequency of $\omega_s = \omega_p - \omega_i$ accordingly. In the beginning, the intensity of pump is much higher than that of signal, along with light propagating through nonlinear crystal, the process mentioned above acts continuously and the energy of pump couples to signal and idler, consequently this is optical parametric amplification. It can be considered to be a down-conversion processing.

In the case of OPA, pump, signal, and idler must meet the energy conservation:

Published on the web February 9, 2013; doi:10.1246/bcsj.20120250

$$\omega_p = \omega_s + \omega_i \quad (1)$$

In order to achieve the best conversion efficiency, wave vectors of pump, signal, and idler should meet the momentum conservation:

$$\vec{k}_p = \vec{k}_s + \vec{k}_i \quad (2)$$

where ω_j and $\vec{k}_j$ are the angular frequency and wave vector with the suffixes j = p, s, and i corresponding to the pump, signal, and idler, respectively.

The phase matching condition in wave corresponds to the momentum conservation in photon in parametric processes including OPA. Typically, phase matching can be satisfied in a birefringent material where the polarizations of the fields and the orientation of the crystal are selected.[4,28] This technique is called angle tuning. BBO (β-BaB_2O_4) is a desirable nonlinear optical crystal especially in UV and visible light range due to its unique features: wide transparency, phase matching ranges, large nonlinear coefficient, high damage threshold, and excellent optical homogeneity.[29,30] For uniaxial crystal, according to the polarization, phase matching is classified into two types: Type-I phase-matching, when the polarizations of signal and idler are in the same direction and Type-II phase-matching when the polarizations are perpendicular. In the negative uniaxial crystal BBO, a type-I (e → o + o) OPA is more suitable for an ultrashort pulse generation than a type-II (e → o + e) OPA because of the smaller group velocity marching (GVM) and larger effective nonlinear coefficient.[4,11,28] Therefore, it provides an attractive solution for various nonlinear optical applications. Phase matching can also be classified into collinear phase matching and noncollinear phase matching according to the propagating direction of pump, signal, and idler. Collinear phase matching usually is applied in picosecond laser systems, because it is easy to achieve higher conversion efficiency when the three waves propagate through longer interacting distance. However, in femtosecond laser systems, not only phase matching but also GVM must be considered to obtain ultrafast pulse, therefore nonlinear phase matching which can provide more parameters to optimize phase matching and group velocity dispersion (GVD) is preferred in our work.

2.2 Broad Band for Phase Matching Condition in Type-I BBO Crystal. The phase mismatch along the pump direction is written in a scalar expression as

$$\Delta\vec{k} = \vec{k}_p - \vec{k}_s \cos\alpha - \cos\beta \quad (3)$$

where α is the noncollinear angle between the wave vectors of the signal and pump, while β is the noncollinear angle between the wave vectors of idler and pump. The relationship among wave vectors of pump, signal, and idler is illustrated in Figure 1.

When $\Delta\vec{k} = 0$, phase matching is satisfied and parametric gain reaches maximum, when $\Delta\vec{k} \neq 0$, parametric gain becomes lower. If in a certain range of wavelength, change of signal wavelength only causes very slight variation of $\Delta\vec{k}$, the gain of signal would not decrease much, and the spectrum are amplified effectively. The band width of this range is called parametric band width. The broader band width can support shorter pulse width according to Fourier transform principle. Therefore the broadening of the parametric band width is an essential condition to obtain a sub-10-fs light source.

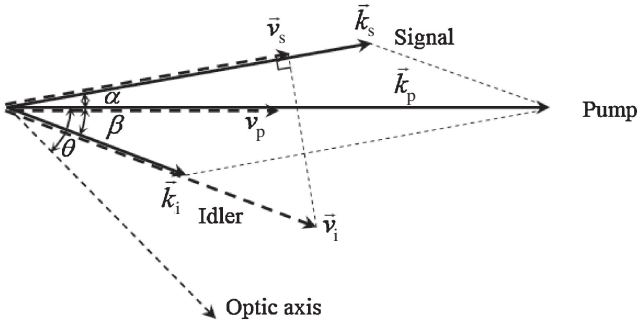

Figure 1. Geometric configuration of the wave vectors in NOPA. $\vec{v}_j$ and $\vec{k}_j$ are the wave vectors (solid lines) and group velocities (thick dashed lines) with the suffixes j = p, s, and i representing the pump, signal, and idler, respectively. θ is phase matching angle, and α and β are internal noncollinear angles.

By Taylor expansion in powers of wavelength around the central wavelength λ_s, Δk is given by

$$\Delta\vec{k}(\lambda) = \Delta\vec{k}_0 + \frac{\partial\Delta\vec{k}}{\partial\lambda_s}\Delta\lambda_s + \frac{1}{2}\frac{\partial^2\Delta\vec{k}}{\partial{\lambda_s}^2}(\Delta\lambda_s)^2 + \ldots \quad (4)$$

Here, $\Delta\lambda_s = \lambda - \lambda_s$ and $\Delta\vec{k}$ is mismatching of three waves at the central wavelength and $\Delta\vec{k} = 0$ in respect that at this wavelength, phase matching is satisfied. Therefore phase mismatching much depends on the second term at right side of equation. It can be considered that if $\frac{\partial\Delta\vec{k}}{\partial\lambda_s} = 0$, change of signal wavelength λ_s has little effects on $\Delta\vec{k}$ thus broad parametric band width can be obtained.

According to Figure 1, the momentum conservation in eq 2 can be expressed in a scalar form in horizontal and vertical direction respectively

$$k_p = k_s \cos\alpha + k_i \cos\beta \quad (5)$$

$$k_s \sin\alpha = k_i \sin\beta \quad (6)$$

Phase mismatching can also be written in the two directions as

$$\Delta k_{//} = k_p - k_s \cos\alpha - k_i \cos\beta \quad (7)$$

$$\Delta k_{\perp} = k_s \sin\alpha - k_i \sin\beta \quad (8)$$

If signal wavelength is the only variable quantity, pump wavelength and noncollinear α angle can be treated as constants, the derivation of eqs 7 and 8 are calculated as

$$\frac{\partial\Delta k_{//}}{\partial\lambda_s} = -\frac{\partial k_s}{\partial\lambda_s}\cos\alpha - \frac{\partial k_i}{\partial\lambda_s}\cos\beta + k_i\frac{\partial\beta}{\partial\lambda_s}\sin\beta \quad (9)$$

$$\frac{\partial\Delta k_{\perp}}{\partial\lambda_s} = \frac{\partial k_s}{\partial\lambda_s}\sin\alpha - \frac{\partial k_i}{\partial\lambda_s}\sin\beta - k_i\frac{\partial\beta}{\partial\lambda_s}\cos\beta \quad (10)$$

Equation 9 multiplied by $\cos\beta$ plus eq 10 multiplied by $\sin\beta$ to obtain:

$$\frac{\partial\Delta k_{//}}{\partial\lambda_s}\cos\beta + \frac{\partial\Delta k_{\perp}}{\partial\lambda_s}\sin\beta = -\frac{\partial k_s}{\partial\lambda_s}\cos(\alpha+\beta) - \frac{\partial k_i}{\partial\lambda_s} \quad (11)$$

As discussed above, if $\frac{\partial\Delta k}{\partial\lambda_s} = 0$ is satisfied, broad parametric bandwidth can be achieved. Therefore let $\frac{\partial\Delta k_{//}}{\partial\lambda_s} = \frac{\partial\Delta k_{\perp}}{\partial\lambda_s} = 0$, eq 11 changes to

$$\frac{\partial k_s}{\partial \lambda_s}\cos(\alpha+\beta)+\frac{\partial k_i}{\partial \lambda_s}=0 \tag{12}$$

Utilizing the relationship between wave vector, group velocity, and wavelength $k=\frac{2\pi n}{\lambda}$, $v=\frac{c}{(n-\lambda\frac{dn}{d\lambda})}$, where c is the vacuum light velocity and n is refractive index, eq 47 can be rewritten as

$$v_s = v_i\cos(\alpha+\beta) \tag{13}$$

Where v_j is the group velocity with the suffixes j = s, i corresponding to the signal and idler, respectively. Equation 13 is the GVM condition, and equivalent to $\frac{\partial \Delta k}{\partial \lambda_s}=0$. The relationship among group velocity of pump, signal, and idler is also shown in Figure 1.

In other words, to obtain broad parametric band width output, the component of group velocity of idler in the direction of signal wave vector must be equal to the group velocity of the signal.

According to eq 12, sum of α and β is expressed as

$$\alpha+\beta=\cos^{-1}\left(-\frac{\partial k_i/\partial\lambda_s}{\partial k_s/\partial\lambda_s}\right)=\cos^{-1}\left(\frac{\lambda_i\frac{\partial n_i}{\partial\lambda_i}-n_i}{\lambda_s\frac{\partial n_s}{\partial\lambda_s}-n_s}\right) \tag{14}$$

From eq 6

$$\frac{\sin\alpha}{\sin\beta}=\frac{k_i}{k_s}=\frac{2\pi n_i/\lambda_i}{2\pi n_s/\lambda_s}=\frac{n_i\lambda_s}{n_s\lambda_i} \tag{15}$$

Expression of noncollinear angle α is

$$\alpha=\tan^{-1}\left\{\frac{\frac{n_i\lambda_s}{n_s\lambda_i}\sin\left[\cos^{-1}\left(\frac{\lambda_i\frac{\partial n_i}{\partial\lambda_i}-n_i}{\lambda_s\frac{\partial n_s}{\partial\lambda_s}-n_s}\right)\right]}{\frac{n_i\lambda_s}{n_s\lambda_i}\left[\frac{\lambda_i\frac{\partial n_i}{\partial\lambda_i}-n_i}{\lambda_s\frac{\partial n_s}{\partial\lambda_s}-n_s}\right]+1}\right\} \tag{16}$$

Here we consider the wavelength λ_s as a parameter, $\lambda_i=(\lambda_p{}^{-1}-\lambda_s{}^{-1})^{-1}$, where λ_p is a constant. Refractive index of signal n_s and n_i idler are functions of wavelength according the Sellmeier equation of BBO

$$n=\sqrt{A+\frac{B}{(\lambda^2+C)}+D\lambda^2} \tag{17}$$

Parameters in eq 17 given in Ref. 31 are used for the calculation: $A=2.7359$, $B=0.01878$, $C=-0.01822$, and $D=-0.01354$. The wavelength dependence which satisfies GVM condition is shown in Figure 2. α has a broad maximum around 600 nm and decreases at shorter wavelength. Over a broader spectral range than 100 nm α suffers only a small deviation of less than 0.06 from 3.7°. The shorter pump wavelength causes blue shift for the GVM range.

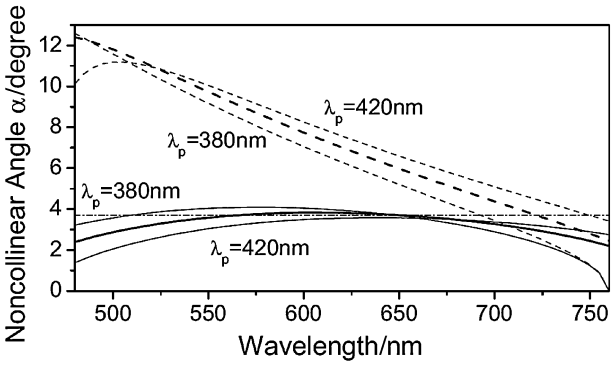

Figure 2. Theoretical noncollinear angle changes according to signal wavelength under GVM conditions. Solid lines represent α and dashed lines represent β. Pump light utilized in simulation are 380, 400, and 420 nm.

2.3 Type-I Phase Matching Condition in BBO Crystal. For type-IOPA realized in BBO crystal, signal and idler are ordinary light, while pump is extraordinary light. Therefore refractive index of signal n_s and n_i idler are only the function of wavelength. n_p is the function of both wavelength and the angle between pump and optic axis θ which is called phase matching angle.

$$n_p(\lambda_p,\theta)=\frac{n_o(\lambda_p)n_e(\lambda_p)}{\sqrt{n_o{}^2(\lambda_p)\sin^2\theta+n_e{}^2(\lambda_p)\cos^2\theta}} \tag{18}$$

where $n_o{}^2(\lambda_p)$ and $n_e{}^2(\lambda_p)$ are principal refractive indices which are only functions of wavelength. n_o and n_e are short for $n_o(\lambda_p)$ and $n_e(\lambda_p)$ respectively in the following expressions.

Introducing $k=\frac{2\pi n}{\lambda}$ into eq 42, phase matching condition can be rewritten as:

$$\Delta k_{//}=\frac{n_p}{\lambda_p}-\frac{n_s}{\lambda_s}\cos\alpha-\frac{n_i}{\lambda_i}\cos\beta=0 \tag{19}$$

The relationship between α and β achieved from eq 8 has been shown in eq 15. By substituting eqs 15 and 18 in eq 19, phase matching angle can be deduced as follows:

$$\theta=\sin^{-1}\left\{\left[\frac{n_0^2n_e^2\lambda_s^2\lambda_i^2}{\lambda_p^2(n_0^2-n_e^2)(n_s\lambda_i\cos\alpha+(n_i^2\lambda_s^2-n_s^2\lambda_i^2\sin^2\alpha)^{\frac{1}{2}})^2}-n_e^2\right]^{\frac{1}{2}}\right\} \tag{20}$$

The curves of θ for various α and β pumped at 400 nm are shown in Figure 3. In this figure theoretical phase-matching curves of θ in a type-I BBO OPA pumped at 400 nm with different values of the signal noncollinear angle α. The signal branches are shown in solid lines while the idler branches are shown in dashed lines. $\alpha=3.7°$ is most appropriate to be used in experiment. For given θ the signal and idler waves can be simultaneously emitted in a broad range of wavelength. For $\theta<29.2°$ the excited range of the spectrum is partially limited, while for $\theta>29.2°$ the whole optical modes at least from 500 nm to 2 μm are excited, which is only restricted by the crystal absorption of idler that rapidly increases at wavelength greater than 2.5 μm (corresponding signal is about 470 nm).[32] These behaviors can be explained by the GVM in a broad sense

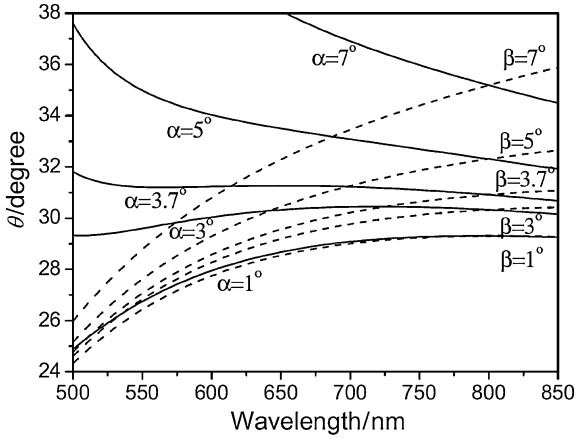

Figure 3. Theoretical phase-matching curves of θ in a type-I BBO OPA pumped at 400 nm with different values of the signal noncollinear angle α. The signal branches are shown in solid lines while the idler branches are shown in dashed lines. $\alpha = 3.7°$ is preferred in experiment, therefore especially shown here.

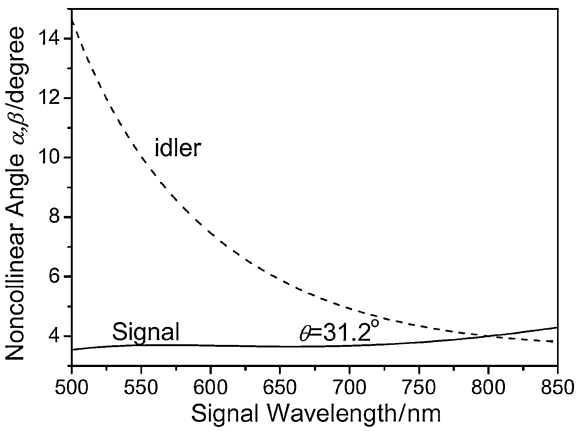

Figure 4. Phase-matching curves of signal and idler in the case of $\theta = 31.2°$, preferred in the present work.

where the appropriate angular dispersions of the noncollinear angles eliminate the GVM between the signal and idler and realizes the ultra-broadband phase matching as shown in Figure 4. Under the fixed phase matching angle $\theta = 31.2°$, noncollinear angle α is almost constant in the range 520 to 720 nm with a standard deviation $\alpha = 3.68° \pm 0.02°$, The mean value and standard deviation of noncollinear β in the same range is calculated as $\beta = 7.34° \pm 2.25°$ which has a relatively large slope. It can be concluded that broadband signal is obtained in exchange for large angular dispersion in idler.

2.4 Optical Parametric Fluorescence. In the case of optical parametric interaction of three waves, if there is no incident signal, the quantum noise could act as signal to interact with pump and yield idler simultaneously. The random quantum noise in any direction can be parametric amplified as long as it satisfies the noncollinear phase matching condition. The amplified quantum noise is called optical parametric fluorescence.[33–35] Under the intense pumping condition, a noncollinear phase-matched optical parametric fluorescence is strongly emitted, sharply favored along a cone-shaped surface

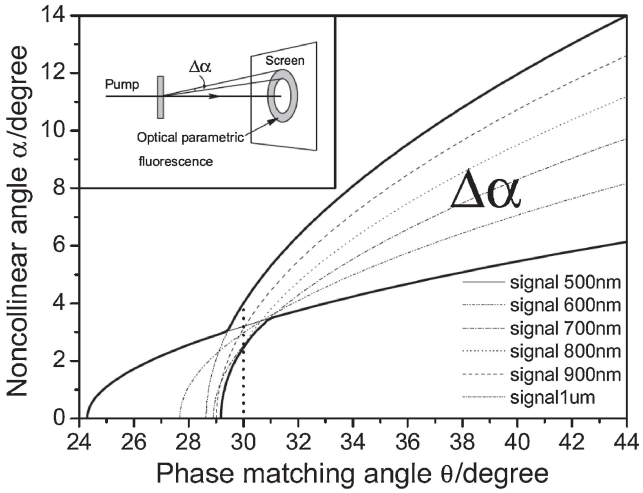

Figure 5. Noncollinear angles α change according to phase matching angle θ in visible spectrum range (from 500 nm to 1 μm). The area between the two thick solid curves is allowable optical parametric fluorescence emitting angle range. Inset illustrates the generation of optical parametric fluorescence.

around the pump beam and form a ring pattern on the plate which is perpendicular to the pump beam due to the type-I interaction as shown in the inset of Figure 5.[2,3] The angular aperture of this taper decreased with decreasing θ until the ring collapsed into a spot when $\theta < 29.2°$ as shown in Figure 5.

The ring structure has a large spectral angular dispersion along the axial direction, which visually exhibits the characteristics of an achromatic down-conversion. For the signal spectrum range from 520 to 720 nm, the dispersions of the fluorescence at $\theta = 31.4°$ and $\theta = 30.8°$ are reversed. The former has larger cone angles and the intensity is higher, because GVM is reduced for larger α^2 (Figure 1). The visible width of the ring according to noncollinear angle α is shown in Figure 5, around $\theta = 30°$, the width of the fluorescence ring reaches the minimum, which provides a powerful tool for adjusting phase matching experimentally.

2.5 Parametric Gain Spectrum. Approximating the plane–wave interaction and neglecting the pump depletion and spectral width, the well-known parametric gain Gin laser amplification is given by[28,36]

$$G = 1 + (gL)^2 \left(\frac{\sinh B}{B}\right)^2$$

$$B = \sqrt{\Gamma^2 - \left(\frac{\Delta k}{2}\right)^2} \cdot L$$

$$\Gamma = 2d_{\text{eff}} \sqrt{\frac{\omega_s \omega_i \Phi}{\varepsilon_0 n_s n_i n_p c^3}} \tag{21}$$

where Γ is the coupling constant, d_{eff} is the effective nonlinear coefficient of the nonlinear optical crystal, ε_0 is the vacuum dielectric constant, Φ is the pump intensity, and L is the crystal length. In the case of $d_{\text{eff}} = 1.6 \cos\theta \,\text{pm V}^{-1}$ and $\Phi = 50$ GW cm^{-2}, the changes of gain according to wavelength with varying noncollinear angle α and phase matching angle θ respectively are calculated as shown in Figure 6.

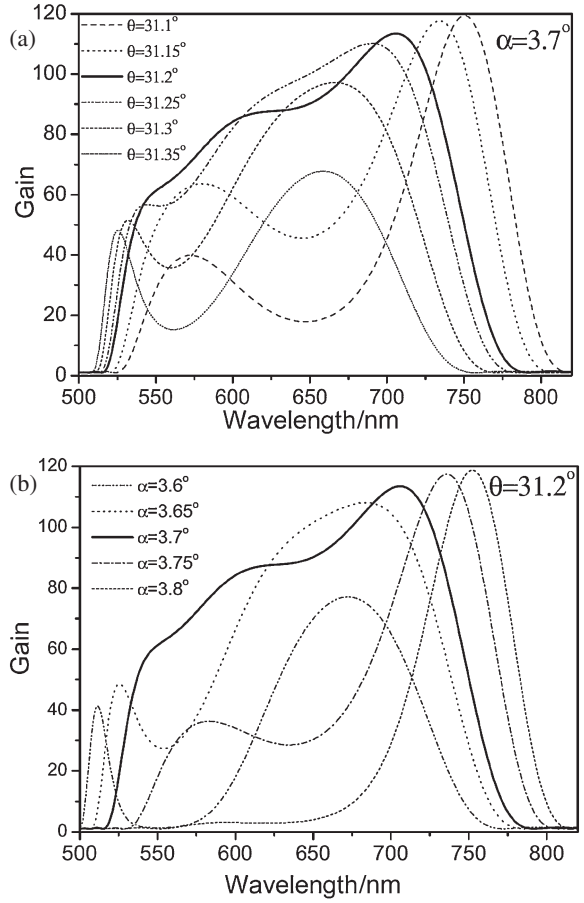

Figure 6. Wavelength dependence of the parametric gain in the type-I noncollinear phase matching condition in BBO crystal. (a) Varying phasing matching angle θ with fixed noncollinear angle $\alpha = 3.7°$; (b) Varying noncollinear angle α with fixed phasing matching angle $\theta = 31.2°$. Thick solid line in both (a) and (b) are the same and considered to be the best simulation.

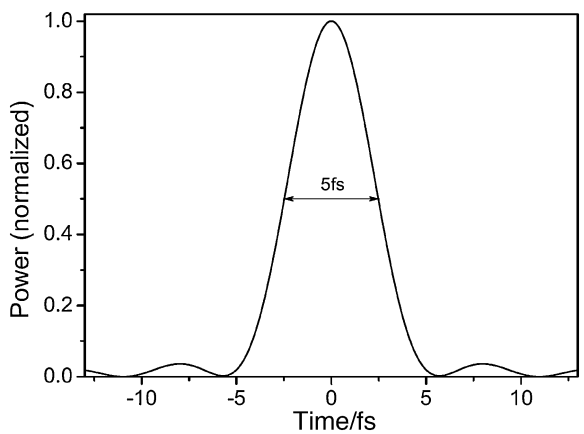

Figure 7. Fourier transform limited pulse of spectrum in Figure 5 with noncollinear angle $\alpha = 3.7°$ and phasing matching angle $\theta = 31.2°$.

Therefore, for broadband signal output, 400 nm light is used in our experiment for pumping BBO crystal in type-I OPA, phase matching angle θ, and noncollinear angle between signal and pump α are chosen for 31.2 and 3.7° respectively. The Fourier limited pulse calculated in the case of $\theta = 31.2°$ and $\alpha = 3.7°$ shows that this broad spectrum can support as short as 5 fs laser pulse as shown in Figure 7. However, the signal pulse generates in BBO crystal with dispersion which needs to be compressed by dispersion compensating elements such as prism pair, chirped mirror, and grating pair.

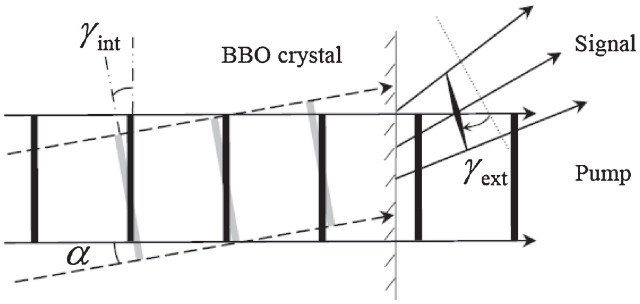

Figure 8. Diagram of the pulse-front tilting between pump and signal in BBO crystal. The thick solid and gray lines represent the pulse front of pump and signal respectively. The thin line with shadow denotes the exit facet of BBO crystal.

The ways of dispersion compensation are relatively sophisticated to obtain ultrashort pulse. Therefore, we focus on another contribution for pulse broadening in BBO crystal during the optical parameter amplification processing in the next section.

2.6 Pulse Width-Pulse-Front Tilting. One of the most important effects on pulse width in NOPA systems is pulse-front tilting, which is an intrinsic effect for the noncollinear interaction of ultrashort pulse.[6,37]

Under the noncollinear geometry, the pulse fronts of the pump and signal cannot perfectly overlap each other as shown in Figure 8. The noncollinear amplification causes tilted gain volume in the signal beam with the noncollinear angle α, resulting in the generation of a tilted signal by the same angle $\alpha = \gamma_{\text{int}}$. The relationship between tilted angles inside and outside of BBO crystal is

$$\tan \gamma_{\text{int}} = \frac{v_s}{c} \tan \gamma_{\text{ext}} \tag{22}$$

Effective beam diameter decreases due to the pulse-front tilting thus the conversion efficiency also decreases. The pulse-front tilting also causes dispersion of the exit angle analogous to light propagating in a prism or grating. Therefore, the pulse-front tilting limits compression of pulse width. However, pulse energy reduction because of amplification saturation due to pump depletion results if the beam size is reduced to decrease the pulse broadening effect. It is concluded that eliminating the pulse-front tilting with a relatively large beam diameter is an effective way to achieve Fourier transform limited pulse with medium pulse energy in NOPA.

There are two ways to optimize pulse front matching, one is pretilting the pulse front of the signal to match with that of the pump in the crystal as shown in Figure 9a, and the other is the pulse front of the pump to match with that of the signal in the crystal as shown in Figure 9b. The second method is preferred because the pulse front needs not be recorrected after amplification.

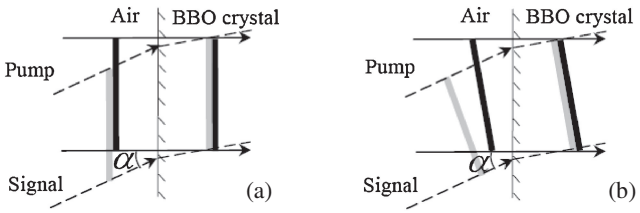

Figure 9. Two schemes for solving the pulse-front mismatching between the pump and signal pulses. (a) Scheme for tilting signal. (b) Scheme for tilting pump.

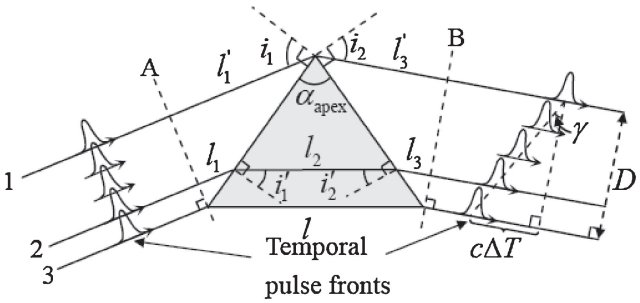

Figure 10. Schematic of the pulse-front tilting by the propagation through a prism. i_1 and i'_1 external and internal incident angles; i_2 and i'_2 external and internal exit angles. D is the beam diameter after the prism. Ray 1 and 3 represent the bound condition for the propagating beam and ray 2 denotes the random ray in this beam. γ is the pulse front tilting angle after propagation in prism.

Utilizing both prism[38] and grating[39] can realize pulse fronts tilting. However the prism is chosen in our experiment since the loss of grating is larger.

As shown in Figure 10, if a bundle of parallel rays propagate through a prism, the length of the optical path between plane A and B are the same for any of the rays according to the Fermat principle:

$$l_1 + nl_2 + l_3 = nl \tag{23}$$

where n and l are refractive index and propagating distance of margin ray in the prism, respectively. Therefore propagation times for any ray from plane A to plane B can be expressed as

$$T_2 = \frac{l_1}{c} + \frac{l_2}{v_g} + \frac{l_3}{c} \tag{24}$$

where c is light velocity in vacuum, $v_g = \frac{c}{n - \lambda \frac{dn}{d\lambda}}$ is the group velocity. Ray 1 and ray 3 are the boundary situation of the beam. The propagation times are:

$$T_1 = \frac{l'_1 + l'_3}{c} = \frac{nl}{c} \tag{25}$$

$$T_3 = \frac{l}{v_g} \tag{26}$$

Considering that a prism is positive dispersion material, the time difference between ray 3 and ray 1 is:

$$\Delta T = T_3 - T_1 = \frac{l\left(n - \lambda \dfrac{dn}{d\lambda}\right)}{c} - \frac{nl}{c} = -\frac{\lambda}{c}\frac{dn}{d\lambda} \tag{27}$$

where λ is wavelength of light.

According to Figure 10, the tilting angle is written as:

$$\gamma = \tan^{-1}\left(\frac{c\Delta T}{D}\right) = \tan^{-1}\left(-\frac{\lambda l}{D}\frac{dn}{d\lambda}\right) \tag{28}$$

where D is the beam diameter after the prism.

The relation for a prism with an apex angle α_{apex} and the Snell's law are

$$\alpha_{apex} = i'_1 + i'_2 \tag{29}$$

$$n = \frac{\sin i_j}{\sin i'_j} \tag{30}$$

where $j = 1, 2$ according to incidence angle and exit angle for the prism, respectively.

Considering i_1 as a constant, differentiation eq 30 in the case of $j = 1$, and utilizing $i'_2 = \alpha_{apex} - i'_1$ deduced from eq 29 yield

$$\frac{\partial i'_2}{\partial \lambda} = -\frac{\partial i'_1}{\partial \lambda} = \frac{\tan i'_1}{n}\frac{dn}{d\lambda} \tag{31}$$

Calculating eq 30 in the case of $j = 2$ in a similar way and combine eq 31

$$\frac{dn}{d\lambda} = \frac{\cos i'_1 \cos i_2}{\sin \alpha_{apex}}\frac{\partial i_2}{\partial \lambda} \tag{32}$$

Paying attention to the following geometric relationship in Figure 10,

$$l \cos i'_1 = \frac{D}{\cos i_2}\sin \alpha_{apex} \tag{33}$$

By substituting eqs 32 and 33 in to eq 28, a simple formula of γ is given by

$$\gamma = \tan^{-1}\left(-\lambda \frac{di_2}{d\lambda}\right) = \tan^{-1}\left(-\lambda \frac{di_2}{dn}\frac{dn}{d\lambda}\right) \tag{34}$$

According to Ref. 40

$$\frac{di_2}{dn} = \frac{n \sin \alpha_{apex}\sqrt{n^2 - \sin^2 i_1}}{\sqrt{1 - [\sin \alpha_{apex}(n^2 - \sin^2 i_1)^{-\frac{1}{2}} - \sin i_1 \cos \alpha_{apex}]^2}} \tag{35}$$

Therefore, if apex angle α_{apex} and light wavelength λ are given, according to eqs 34 and 35, expected wave front tilting angle γ can be obtained by adjusting incidence angle i_1.

The prism of pulse front tilting is usually set before OPA, so called "pretilting." It was first applied by Danielius's group in 1996 in a collinear OPA.[41]

2.7 Experimental Setup. 2.7.1 NOPA Setup: According to the basic theory mentioned above, the experimental setup of NOPA is illustrated in Figure 11. The pump source of this NOPA system is a commercially supplied regenerative amplifier (Spectra Physics, Spitfire), whose central wavelength, pulse duration, repetition rate, and average output power were 800 nm, 50 fs, 5 kHz, and 750 mW, respectively. The input light is separated into two beams; the first beam propagates through 2-mm thick sapphire to generate white-light continuum for seed of signal. A cutoff filter which blocks wavelengths longer than 750 nm is placed after sapphire in order to prevent the intense spike around 800 nm. The second beam propagates through a 0.4 mm-thick BBO crystal (29.2°z-cut) to yield second har-

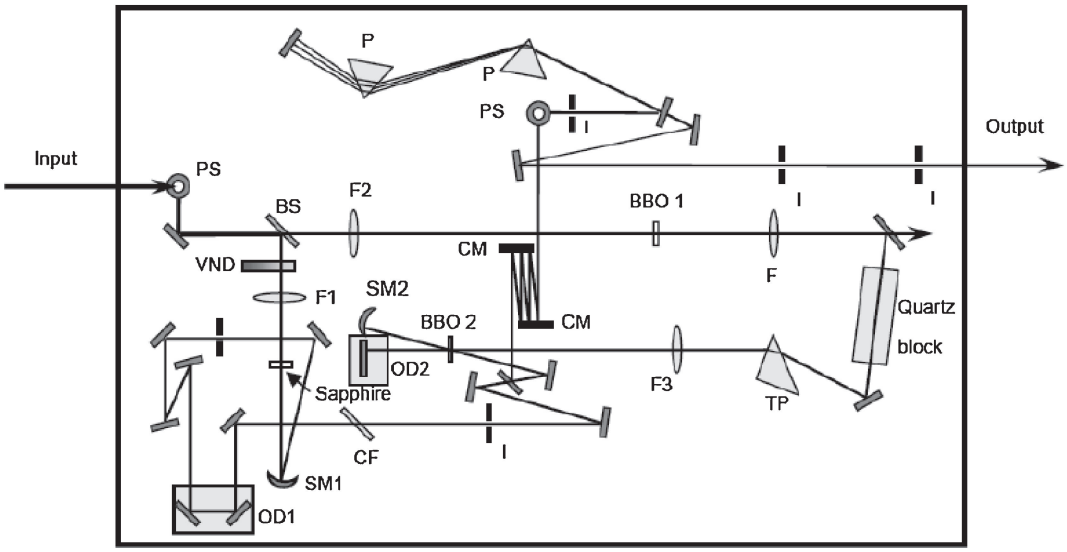

Figure 11. Diagram of NOPA system. PS, Periscope; BS, beam splitter; VND, Variable neutral-density filter; F's, Focusing lens (F1: $r = 100$ mm; F2: $r = 400$ mm; F3: $r = 250$ mm); SM's, Spherical mirrors (SM1: $r = 120$ mm; SM2: $r = 100$ mm); I, iris; Sapphire: to obtain broad band signal from 450 nm; BBO 1, to generate second harmonic light for signal; BBO 2, use for noncollinear parametric amplification; Quartz block, for pulse stretching; CF, cutoff filter (cut to 750 nm); OD1, adjustable optical delay line for first path OPA; OD2, adjustable optical delay line for second path OPA; TP, prism for pulse-front tilting; cm, chirped mirror; P, prism; The elements without label are plane mirrors.

monic light for pump of NOPA following type-I ($o + o \rightarrow e$) phase match conditions. In order to achieve effective and stable optical parametric amplification, a quartz block is used to stretch pump pulse to 200 fs to be comparable to white-light continuum. A prism with 45°apex is arranged after the quartz block for pretilting the pulse front of the pump to match that of the signal in the crystal. Then the pretilted pulse is focused to a 1-mm thick BBO crystal (31.5°z-cut) overlap spatially with white-light continuum beam. The optical delay line (OD1) in white-light continuum beam path is adjustable for temporal overlapping. In order to achieve higher signal energy, the remained pump and signal are reflected after the first OPA processing and focus again in BBO crystal at a lower position. The temporal overlapping of pump and signal can be regulated by the optical delay line (OD2) in the pump beam path.

The amplified signal just after BBO crystal is around 0.3 μJ. A pair of ultra-broadband chirped mirrors was designed to compensate group delay (GD), group delay dispersion (GDD), and third-order dispersion (TOD) in NOPA system and followed by a pair of prisms. One of the chirped mirrors exhibits a GD property with several reflections to compensate the chirp of the NOPA output with the combination of the prism pair, air and the beam splitter with the spectral region from 480 to 760 nm. The other one was designed to have a GDD and TOD with $-45\,fs^2$ and $20\,fs^3$ with the spectral region from 500 to 780 nm. These chirped mirror pair and prism pair compose the compressor. The chirped mirrors have high reflectivity ($R >$ 99%) while the prism pair mainly gives loss in our case. The spectrum is adjustable by changing the noncollinear angle α. The best noncollinear angle α was judged by adjusting the fluorescence ring width to the thinnest one experimentally. The pulse width could be as short as 5 fs with the spectrum 520–720 nm theoretically. However, in some experimental cases, the spectrum of NOPA was adjusted to the longer wavelength extending from 556 to 753 nm in order to achieve higher absorbance of some sample. The pulse width in this case is 7 fs which slightly broader than the optimum case.

2.7.2 Pump–Probe Experimental Setup: A pump–probe experimental setup is shown in Figure 12. For pump–probe experiment, the output from the NOPA is separated into pump and probe beams by a beam splitter at a ratio of 5:1. A frequency divider is synchronized with NOPA and controls the chopper at 2.5 kHz which is half the frequency of NOPA. Both pump and probe beams are focused on the surface of sample about 50 μm in diameter with a 127 mm (0.5 inch) parabolic mirror. The spatial overlap of pump and probe beams on the sample is checked with a 0.1 mm diameter pinhole. The transmission of the probe beam is received by the fiber.

There are two computers for different purposes: PC1 is used for measuring pulse width from NOPA before pump–probe experiment and real-time monitoring stability of NOPA during experiments. Pump and probe beams are spatially overlapped in a BBO crystal on a sample stage to generate the sum frequency. By motor driving the optical delay line in pump beam path (OD3), the autocorrelation of pump and probe can be measured and thus the pulse width from NOPA is able to be checked before pump–probe experiments.

The second computer (PC2) is prepared for recording the DC (laser and transmitted spectrum) and AC (ΔT) from multilock-in amplifier. The signal is spectrally dispersed using a polychromator (Jasco, M25-TP) over 128 channels with a spectral resolution of 1.5 nm and each channel was detected by an avalanche photodiode in conjunction with a lock-in amplifier locked onto the 2.5-kHz reference frequency set by an optical chopper that modulated the pump beam. The detecting range is slightly variable according to NOPA spectrum by changing

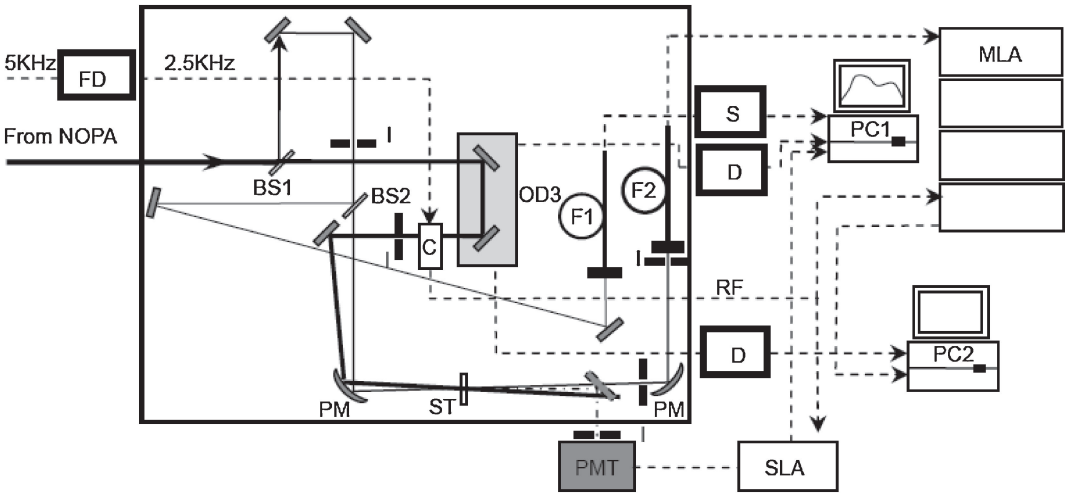

Figure 12. Diagram of pump–probe setup. Solid lines represent beam path and dashed lines denote electric connection among equipment. BS's, beam splitter; OD3, adjustable optical delay line for pump; C, chopper; I, iris; PM, parabolic mirror; F's, fiber for signal detecting; PC's, computer; PMT, photomultiplier tube; D, optical delay controller; S, spectrometer; SLA, signal lock-in amplifier; MLA, multi lock-in amplifier. ST, the position for BBO crystal to measure autocorrelation of pulse and setting the sample. The elements without label are plane mirrors. The elements and light in dash dot line are used for autocorrelation measurement.

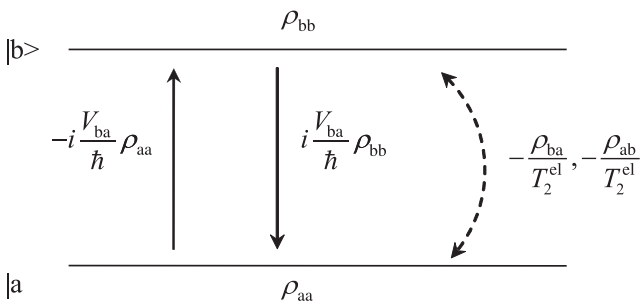

Figure 13. Diagram of atom transition between a two-level system. Electronic transition takes place from the ground state |a⟩ to the excited state |b⟩ when absorbing a phonon while when the photon is emitted, it takes place from the excited state to the ground.

the angle of dispersed grating inside. PC2 is also connected to control OD3 for changing the delay time and measure the data ($\Delta T(t)$). The polarization of both pump and probe are horizontal.

2.8 Conclusion. Several key techniques of NOPA were represented in this Chapter. The NOPA system is based on the optical parametric down-conversion principle. Both the energy conservation and momentum conservation are thought to achieve the broad band parametric gain spectral range. In order to obtain the broad parametric bandwidth output, the component of group velocity of idler in the direction of signal wave vector must be equal to the group velocity of signal. Phase matching angle and noncollinear angle are two important parameters of phase matching conditions. The optimized phase matching angle and noncollinear angle were calculated to $\theta = 31.2°$, $\alpha = 3.7°$, respectively in the case of 400 nm pump light. Under these conditions, the parametric gain spectrum was obtained as broad as 200 nm (from 520 to 720 nm), which can support 5 fs FT limited pulse.

Optical parametric fluorescence is an accompanying phenomenon in parametric amplification processing if the quantum noise acts as signal to interact with pump and yield idler simultaneously. The optical parametric fluorescence ring can be observed if the pump intensity is high enough. From the calculation of the ring width, it was found that around the optimized phase matching angle and noncollinear angle, the ring width becomes minimum. It is a guidance to adjust both of the angles experimentally.

The compressor, which consists of a chirped mirror pair and prism pair was applied to compensate the first and higher order GD. An intrinsic effect for the noncollinear interaction of ultrashort pulse called pulse-front tilting causes the pulse fronts of the pump and signal to imperfectly overlap. Therefore, another prism was used to cause pretiling of pump, and then improve the pulse front overlapping condition in BBO crystal.

According to the theory above, NOPA was set up experimentally. A pulse as short as 7 fs with the spectrum of 556–753 nm was obtained and utilized in pump–probe experiments. In pump–probe experiments, in order to detect the broad band spectrum from NOPA, a multilock in amplifier was applied.

In the following chapter, we start to discuss the fast dynamics in a molecule using the pump–probe experiment with the NOPA as the light source.

3. Theory of Pump–Probe Experiment

3.1 Theory of Interaction between Laser Field and a Two-Electronic-State System. To discuss the principle of pump–probe experiments of molecules at first we would like to describe a simple model of a two-electronic-state system and coherent light in the beginning and then go to a more complicated system with electronic states coupled to multilevel vibrational levels forming a multilevel structure.

For two-level energy system, the time evolution of the system is described by the 2-by-2 density matrix ρ which satisfies the Bloch equation with all operators written in the

rotating reference frame:

$$\frac{\partial \rho}{\partial t} = \frac{1}{i\hbar}[\hat{H} + \hat{V}(t), \rho(t)] + \frac{\partial}{\partial t}\rho_{\text{relax}} \tag{36}$$

Where $\rho = \begin{bmatrix} \rho_{aa} & \rho_{ab} \\ \rho_{ba} & \rho_{bb} \end{bmatrix}$ is the density matrix, the vibronic Hamiltonian $\hat{H}$ is perturbed by the dipolar Hamiltonian of interaction with the pump light pulse $\hat{V}$.

The elements of the density matrix ρ is described by

$$\dot{\rho}_{ba}(\vec{r},t) = -\left(i\Omega + \frac{1}{T_2^{el}}\right)\rho_{ba}(\vec{r},t) + \frac{1}{\hbar}V_{ba}(\vec{r},t)[\rho_{bb}(\vec{r},t) - \rho_{aa}(\vec{r},t)] \tag{37}$$

$$\rho_{ab}(\vec{r},t) = \rho^*_{ba}(\vec{r},t) \tag{38}$$

$$\dot{\rho}_{bb}(\vec{r},t) - \dot{\rho}_{aa}(\vec{r},t) = -\frac{[\rho_{bb}(\vec{r},t) - \rho_{aa}(\vec{r},t) - (\rho_{bb}(\vec{r},t) - \rho_{aa}(\vec{r},t))_0]}{T_1^{el}} + \frac{2i}{h}[V^*_{ba}\rho_{ba}(\vec{r},t) - V_{ba}\rho^*_{ba}(\vec{r},t)] \tag{39}$$

Where T_1^{el} and T_2^{el} are the electronic population decay time and electronic dephasing time, respectively; $[\rho_{bb}(\vec{r},t) - \rho_{aa}(\vec{r},t)]_0$ is the equilibrium population difference at zero laser field, and Ω is the detuning between the pump field at frequency ω_1 and the transition frequency ω_{ba} (i.e. $\Omega = \omega_{ba} - \omega_1$).

The interaction potential $V_{ba}(\vec{r},t)$ is given by

$$\vec{V}_{ba}(\vec{r},t) = -\vec{\mu}[\vec{E}_{pu}(t)\exp(i\vec{k}_{pu}\vec{r}) + \vec{E}_{pr}(t)\exp(i\vec{k}_{pr}\vec{r})] \tag{40}$$

Here $\vec{\mu}$ is the dipole moment, $\vec{E}_{pu}(t)$ and $\vec{E}_{pr}(t)$ are the time envelopes of the pump and probe fields, respectively, which have parallel polarization in our case.

The perturbation technique can be applied to solve eq 37 in case of that Rabi frequency $\Omega_R = 2\vec{\mu}\vec{E}_{pu}/\hbar$ is smaller than $1/T_2^{el}$. This is done by solving to second order in the pump field and to first order in the probe field. Until this point the electronic structure of interest is a two-electronic-state system. From here we switch gear to a more complicated system with electronic states coupled to multilevel vibrational levels forming a multilevel structure as a whole. Then under the Condon approximation details of which are described in the next subsection, the macroscopic electric polarization of the two vibronic states (ground state and one excited singlet state) can be simply described by the direct product of the pure electronic macroscopic electric polarization and the Franck–Condon factor associated with all the possible molecular vibrational normal modes. Then the procedure of the transient transmittance change can be straightforward as described below.

The time envelope of the macroscopic electric polarization $\vec{P}^{(3)}_{pr}(t)$ after factorizing out the Franck–Condon factor except the vibrationally time dependent part in a molecular vibronic system propagating in the probe direction is given by the following equations.[42]

$$\begin{aligned}\vec{P}^{(3)}_{pr} = {} & [\rho_{bb}(\vec{r},t) - \rho_{aa}(\vec{r},t)]_0 \int_{-\infty}^{+\infty} dt_3 A_2(t_3) \\ & \times \left\{ \vec{E}_{pr}(t-t_3)\int_{-\infty}^{+\infty} dt_2 A_1(t_2)\left[\vec{E}_{pu}(t-t_3-t_2)\int_{-\infty}^{+\infty} dt_1 A_2(t_1)\vec{E}^*_{pu}(t-t_3-t_2-t_1)\right.\right. \\ & \left. - \vec{E}^*_{pu}(t-t_3-t_2)\int_{-\infty}^{+\infty} dt_1 A_2(t_1)E_{pu}(t-t_3-t_2-t_1)\right] \\ & + \vec{E}_{pu}(t-t_3)\int_{-\infty}^{+\infty} dt_2 A_1(t_2)\left[\vec{E}_{pr}(t-t_3-t_2)\int_{-\infty}^{+\infty} dt_1 A_2(t_1)\vec{E}^*_{pu}(t-t_3-t_2-t_1)\right] \\ & \left. - \vec{E}_{pu}(t-t_3)\int_{-\infty}^{+\infty} dt_2 A_1(t_2)\left[\vec{E}^*_{pu}(t-t_3-t_2)\int_{-\infty}^{+\infty} dt_1 A_2(t_1)E_{pr}(t-t_3-t_2-t_1)\right]\right\}\end{aligned} \tag{41}$$

$$A_1(t) = A_2(t) = 0 \quad (t < 0) \tag{42}$$

$$A_1(t) = \frac{2i\mu}{\hbar}\exp(-t/T_1^{el})\exp(-i(\omega_v t + \tan^{-1}((\omega - \omega_e + \omega_v)T_{vib}))) \quad (t > 0) \tag{43}$$

$$A_2(t) = \frac{i\mu}{\hbar}\exp(-t/T_2^{el})\exp(-i\Omega t)\exp(-t/T_2^{vib})\exp(-i(\omega t + \tan^{-1}((\omega - \omega_e + \omega_v)T_{vib}))) \quad (t > 0) \tag{44}$$

Here T_{vib} is the vibrational period, T_2^{vib} is the vibrational dephasing time, ω_v is the vibrational frequency, and ω_e is the frequency corresponding to the 0–0 transition energy from the ground to the excited electronic state.

The difference absorbance $\Delta A(\omega)$ of the system, in the frequency domain is proportional to the differences of the imaginary part of susceptibilities which can be obtained by Fourier transform of $P^{(3)}_{pr}$

$$\Delta A(\omega) \propto \text{Im}\left[-\frac{F(P^{(3)}_{pr})}{E_{pr}(\omega)}\right] \tag{45}$$

Where $F(P^{(3)}_{pr})$ denotes the Fourier transform of $P^{(3)}_{pr}$, and the division by $E_{pr}(\omega)$ make the signal independent of the probe spectrum.

3.2 Physical Interpretation of the Theory. The difference absorption spectrum has three distinct polarization components, as described by eq 41.

The difference spectrum corresponding to the first term, which is called "population term" and appears only in the positive-time range where the pump comes before the probe, is proportional to the changes in population difference between the two states, which is induced by the pump pulse via a dipole transition. This is the only term that persists when the probe follows the pump, and it decays with a time constant of T_1^{el}.

This process is induced by the generation of the third-order nonlinear polarization by the temporal sequence of the fields of pump–pump–probe.

There are three mechanisms contributing to the first term: First, the temporal behavior of the transmitted light intensity caused by pump pulse induces population changes in the electronic states. The electronic states can be excited states or some intermediate states of chemical reaction triggered by the pump pulse. Second, the modification of transition probability due to the time-dependent Franck–Condon overlap by the nuclear wave-packet formation also can effect this term. The nuclear wave-packet is vibrationally "coherent" on the potential surface of the electronic state generated by pump pulse and becomes electronically incoherent after the electronic dephasing time. This means that the final state of transition induced by the femtosecond pump pulse is the diagonal terms of the density matrix of the electronic states. Third, the change in the refractive index induced by the molecular vibration can be also considered as one origin of the first term. This is a kind of induced phase modulation, sometimes called "molecular phase modulation." This is again vibrationally "coherent" on the potential surface of electronic excited state generated "electronically incoherently." As mentioned before this term is called the population (= electronic diagonal) term and it can exist when there is no population change but if there is coherent molecular vibration. The coherent vibration is due the term factorized out from the nonlinear macroscopic electronic polarization in eq 41.

The second term in eq 41 takes place by pump–probe–pump sequence in the generation of the third-order polarization. This is called the pump polarization coupling term and is proportional to the pump-induced polarization that occurs when the probe pulse arrives at the same time as the pump pulse. The probe field interacts with the pump polarization to create a grating due to spatial modulation of the level populations. The pump field then interacts with the grating to create a polarization component spatially coherent with the probe field. It is effective only when the pump pulse overlaps the probe pulse in time, since it requires the presence of the pump field both before (to create the grating) and after (to be diffracted by the generated grating into the probe direction) the arrival of the probe pulse.

The third term, which is called the perturbed free-induction decay term, occurs in the negative-time range where the probe precedes pump, because the pump field modifies the otherwise free decay of the probe-induced polarization: The preceding probe pulse generates macroscopic coherent electronic polarization, and then an intense pump field arrives at the sample and interferes with the probe-generated polarization resulting in the formation of the grating. Another electric field component of the pump pulse is diffracted by the grating into the direction of the probe pulse. Therefore it persists when the probe precedes the pump, remains finite and decays exponentially with an exponential time constant of T_2^{el}, which includes both homogeneous and inhomogeneous decay.

Even though the above classification is made in three groups: (1) the pump preceding case, (2) pump–probe overlapping case, and (3) probe preceding case, in a real experiment the second case there is overlap between the pump pulse and probe pulse there is a contribution not only of pump polarization coupling but also of perturbed free-induction decay term, and population term. The sum of two contributions due to pump polarization coupling and perturbed free-induction decay term can be either constructive or destructive depending on the sign of the two signals. The coherence term is given by the convolution function of pump and probe pulse and gives no contribution outside of the function. Therefore, the decay in the negative time direction at some wavelengths can be steep due to dominant contribution of coherent term with a minor contribution of perturbed free induction decay term. Especially this effect becomes substantial when the coherent coupling term has an opposite sign to that of the perturbed decay term. Another effect can happen in the opposite direction at different probe wavelength. Therefore size and sign of the third term is probe wavelength dependent due to two possibilities: The first one is that the perturbed free induction decay is the process of the relaxation of macroscopic polarization corresponding to the transition between the excited vibronic state and the ground state. Then the sign of ΔA and its decay are then dependent on the relevant vibronic state belonging to the same electronic excited state.

The perturbed free-induction decay term can be used to determine the electronic phase relaxation time and study vibrational phase relaxation in excited electronic state(s). If the frequency of the mode is high enough, there is no population of vibrational levels higher than $\nu = 0$. Therefore, the polarization induced by the probe pulse $\vec{P}_{\mathrm{pr}}(t)$ in such a case is the vibronic polarization associated with the transition from the lowest vibrational level ($\nu = 0$) in the electronic ground state to the vibrational excited level.

3.3 Principles of Real-Time Vibration Spectroscopy: Modulation of Electronic Transition Probability by Wave-Packet Motion. This section describes the principles of real-time vibrational spectroscopy mainly in the third time regime discussed in the previous section. Real-time traces represent the time-dependent intensity being modulated by wave packet motion generated by the intense pump pulse, whose duration is shorter than the molecular vibrational period.

There are two methods of studying vibrational dynamics in excited electronic (or excitonic) states in condensed matter. One is the analysis in frequency-domain; the other is in time-domain. Most frequently used methods are the former and they are time-resolved Raman scattering spectroscopy and time-resolved infrared absorption spectroscopy. The latter is real-time vibration spectroscopy, used to get information of real-time amplitude of vibration through modulation of the electronic transition probability, including the vibrational initial phase after impulsive excitation. They can also provide information of the vibronic coupling strength and dynamics of the vibrational modes in both ground and excited electronic states. Thus the relaxation of electronic states and the dynamics of vibrational levels can be studied with the same experimental equipment under exactly the same conditions. They have been used in the real-time vibrational spectroscopy of many molecular and polymer systems.[24–26]

In most molecular systems, the wave function of a molecular electronic state can be factorized into the electronic part with nuclear coordinates as parameters and the nuclear component using the Born–Oppenheimer approximation, except when the electronic state has degeneracy:

$$\Psi(q, Q) = \Phi(Q, q)\chi(Q) \quad (46)$$

Here, q and Q represent the electron and nuclear coordinates, respectively. The transition dipole between two electronic states under the Born–Oppenheimer approximation is given by the following if the Condon approximation is satisfied:

$$\begin{aligned}&\langle\Psi_1(q, Q)|eq|\Psi_2(q, Q)\rangle_{Q,q}\\ &= \langle\chi_1(Q)\langle\Phi_1(Q, q)|eq|\Phi_2(Q, q)\rangle\chi_2(Q)\rangle\\ &\cong \langle\Phi_1(Q, q)|eq|\Phi_2(Q, q)\rangle\langle\chi_1(Q)|\chi_2(Q)\rangle \quad (47)\end{aligned}$$

The origins of the intensity modulation can be classified into two cases: when the Condon approximation is satisfied and when it is not satisfied. The former case is due to the time-dependent Franck–Condon (FC) overlap as a result of wave packet formation, the wave function of which is a linear combination of the wave functions of the relevant vibrational levels. The latter case occurs when the electronic wave function is mixed with a third electronic state, which causes the electronic transition probabilities to be exchanged between the relevant two states. Following the wave-packet motion, the molecular structure is deformed and the corresponding electronic wave functions and electronic energies of these states are modified resulting in the modulation of the transition probability.

4. An Example of Real-Time Spectroscopy: Primary Conformation Change during the Primary Photoisomerization in Bacteriorhodopsin

4.1 Introduction. Photoisomerization of rhodopsin is the key reaction in the vision process in vertebrates. However, ultrafast time-resolved observation of this process is difficult because rhodopsin does not recover after in vitro photobleaching in many opsins except rare examples such as squid.[43–45] On the other hand the membrane protein bacteriorhodopsin (bR),[42,46] which is extracted from bacteria, is more stable than rhodopsin and even artificial chemicals, making it a promising functional material for optical memories and switches.[47] The physiological function of bR in live bacteria is proton pumping to produce a chemical potential for ATP synthesis. This pump is optically triggered by *trans–cis* photoisomerization, which is closely related to *cis–trans* photoisomerization of rhodopsin in the vision process[48] even though the reaction is in the opposite direction. Because of these interesting physiological and artificial functionalities, the primary process of bR has been extensively studied both theoretically[49,50] and experimentally.[51–57]

Most studies made up to now[42] consider the primary photoprocess to be described as follows:

$$\text{bR} \rightarrow \text{H} \text{—(200 fs)} \rightarrow \text{I} \text{—(500 fs)} \rightarrow \text{J} \text{—(3 ps)} \rightarrow \text{K} \quad (48)$$

However, some controversial experimental results have been reported. For example, Ruhman's group showed experimentally that the locked retinal chromophore contained in bR exhibits a similar photoinduced spectral change to that of ordinary bR.[58,59] Atkinson's group claimed that the long-accepted isomerization process does not occur in the primary process, even in the J intermediate.[60] The J intermediate is often assigned as a ground-state species in which the retinal chromophore is isomerized to a 13-*cis*-configuration, as first proposed by the group of Ruhman.[58]

Furthermore, two theoretical models of photoisomerization have been proposed, namely a two-state, two-mode model and a three-state model proposed by groups of Olivucci[49,61] and Schulten;[50,62] it still remains unclear which model is correct. Recent studies of photoisomerization of retinyl chromophore have shed light on the dynamics after photoexcitation;[63,64] however, the details of the transient states still remain contentious.

Electronic and molecular vibrational structures of transient intermediate species in photoisomerization can be revealed by ultrafast laser spectroscopy using ultrashort laser pulses, as has been performed for chemical reactions.[65,66] Ultrafast spectroscopy is complementary to the X-ray diffraction technique proposed by the group of Anfinrud[67] and the electron diffraction methods used by groups of Miller[68] and Zewail.[69]

In the present study, the vibrational amplitude is detected with a subfemtosecond resolution due to the short pulse duration and the high signal-to-noise ratio. Ultrafast spectroscopy offers much higher time resolutions than electron and X-ray diffraction experiments. In addition, it can be used for the measurements of amorphous materials and liquids, which are difficult to analyze by X-ray or electron diffraction. In a previous paper by us,[70] measurements of time-resolved difference absorption spectrum resolving the real-time dynamics of the amplitude of molecular vibration could elucidate the ultrafast change in the frequencies of in-plane and out-of-plane bending modes associated with molecular structural changes during photoisomerization.[70] By this method even the information of transition states could be obtained via the instantaneous vibrational frequency.[70] Femtosecond stimulated Raman spectroscopy that has high temporal and spectral resolution was used to observe time-dependent conformational changes.[71] However, femtosecond stimulated Raman spectroscopy measures only the vibration intensity and hence it cannot provide any information on the vibrational phase, which can be obtained by real-time measurements of vibrational modulation of difference absorbance. The analysis using vibrational phase makes it possible for the wave packet associated with the ground state to be distinguished from those with the excited state. Also the real-time observation can provide information of very rapidly changing vibrational frequency which is changing in the time scale of vibrational period. Then the molecular structural change associated with such a fast reaction can be monitored by the real-time observation of the vibrational amplitude detection through the modulation of the instantaneous modulation of the electronic transition.

As discussed in the previous section and in our recent study,[72] time-resolved difference absorption includes contributions of wave packets on the potential surfaces of both electronic ground state and one or several excited states. There are three ways to distinguish a signal due to the ground state wave packet from that of an excited state. The first method is time-resolved spectroscopy using chirped pump pulses, which was performed by Kahan et al.[58] The second method is to observe the vibrational phase of a molecular vibration. The motion of a ground-state wave packet commences from a stable local minimum point on the ground-state potential-energy surface, whereas an excited-

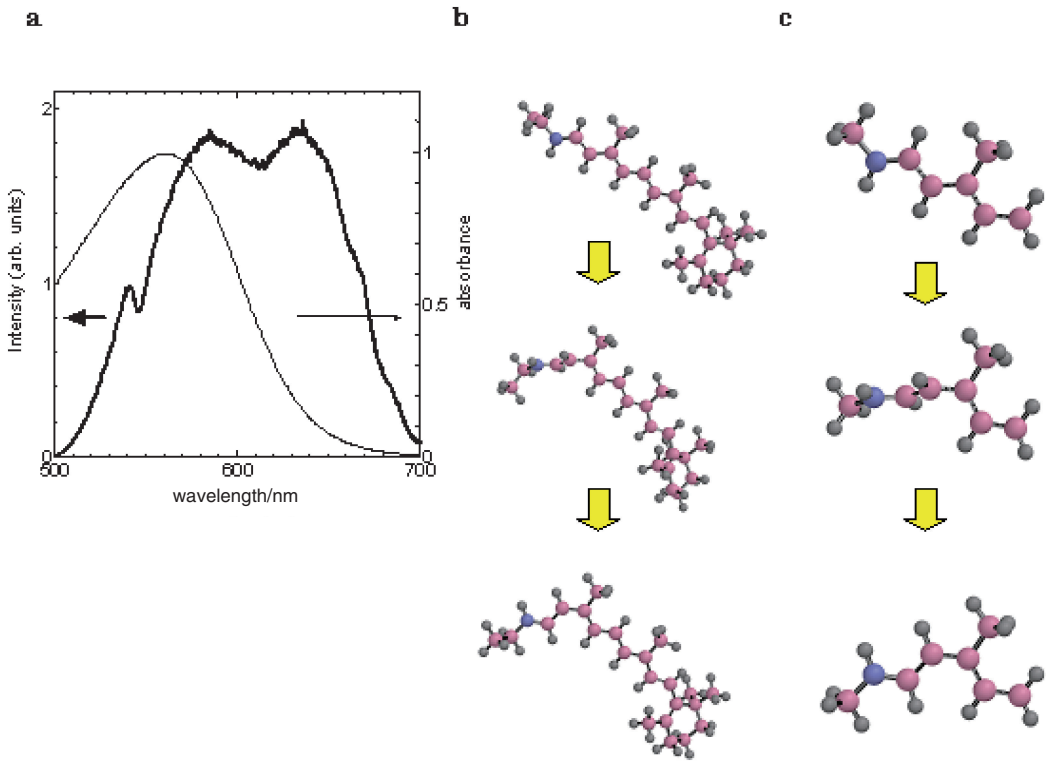

Figure 14. Laser output spectrum from NOPA, absorption spectrum of bR, and molecular structure of the retinal chromophore in bR. (a) Laser spectrum (thick line) and absorption spectrum of bR (thin line). (b) Schematic conformational change in the *trans–cis* photoisomerization of the retinal chromophore in bR (calculated by CIS/6-31G*//CIS/6-31G*) (1). (c) Enlarged views of molecular structures around C_{13}=C_{14} and C_{15}=N shown in (b). The purple and blue balls in (b) and (c) represent carbon and nitrogen atoms, respectively. The first, second, and third models from the top to the bottom in (c) are exhibiting the chromophore structure in H, I, and J states, respectively.

state wave packet starts its motion from the Franck–Condon state toward a local minimum point on the excited-state potential-energy surface. Therefore, vibrations of wave packets on the potential surfaces of the ground and excited states are expected to be sine-like and cosine-like, respectively. The third method is to observe the dependences of the signal on the probe wavelength and the delay. Using intermediate lifetimes determined in previous studies, decay of the transient absorption signal can determine the dominant intermediates in different probe wavelength regions. The sign of the signal also helps assign the origin of the signal: a negative absorbance change indicates that photobleaching is caused by depletion of the electronic ground state or stimulated emission from the excited state, whereas a positive absorbance change indicates induced absorption from the first excited state to a higher excited state. In the present study, we describe the ultrafast processes in bacteriorhodopsin and oxyhemoglobin using ultrashort pulses to study the mechanisms of very efficient photoisomerization and photodissociation, respectively, in these systems.

4.2 Experimental. Bacteriorhodopsin, bR, was suspended in water buffered at pH 7 without any detergent. The absorption spectrum of a bR sample (optical density per 1-cm OD being 10.6 at the 560-nm peak) in a 1-mm cell, and the laser spectra are shown in Figure 14a. The observed absorption spectrum with a peak at 562 nm confirms that the sample used in this work consists mainly of the all-*trans*-structure. Figures 14b and 14c, show the calculated structures of the retinal chromophore, which introduces the schematic mechanism of the *trans–cis* photoisomerization of the retinal chromophore. Models 1, 2, and 3 from the top to the bottom in Figure 14c are related to the structures of the H, I, and J states, respectively. Pump–probe signals were detected with a 128-channel lock-in amplifier. The pulse energy and peak intensity of the pump pulses at the sample were ca. 10 nJ and 10 GW cm^{-2}, respectively, which are ca. 10 times higher than the probe pulses. The laser spectrum is also shown in Figure 14a showing the excitation of the sample bacteriorhodopsin can be efficiently excited with remaining space in its spectrum to monitor the spectra of both the excited state and intermediate species.

4.3 Results and Discussion. The experimental result of real-time traces probed at 128 different wavelengths is displayed two-dimensionally in Figure 15. It covers the wavelength range of 505–665 nm. The obtained data reveal the detailed photoexcited dynamics of the retinal chromophore in bR during photoisomerization. This technique has the potential to overcome the problems associated with the other two methods mentioned namely time-resolved IR absorption and time-resolved Raman spectroscopy. This figure contains a lot of information about the sample dynamics, which can be obtained from quasi-continuous spectra and time-dependent (including vibrational phase) transmittance changes at all wavelengths. Simultaneous measurement at all the probe wavelengths enables measurements to be performed much faster than previous time-consuming measurements at five different wavelengths.[51]

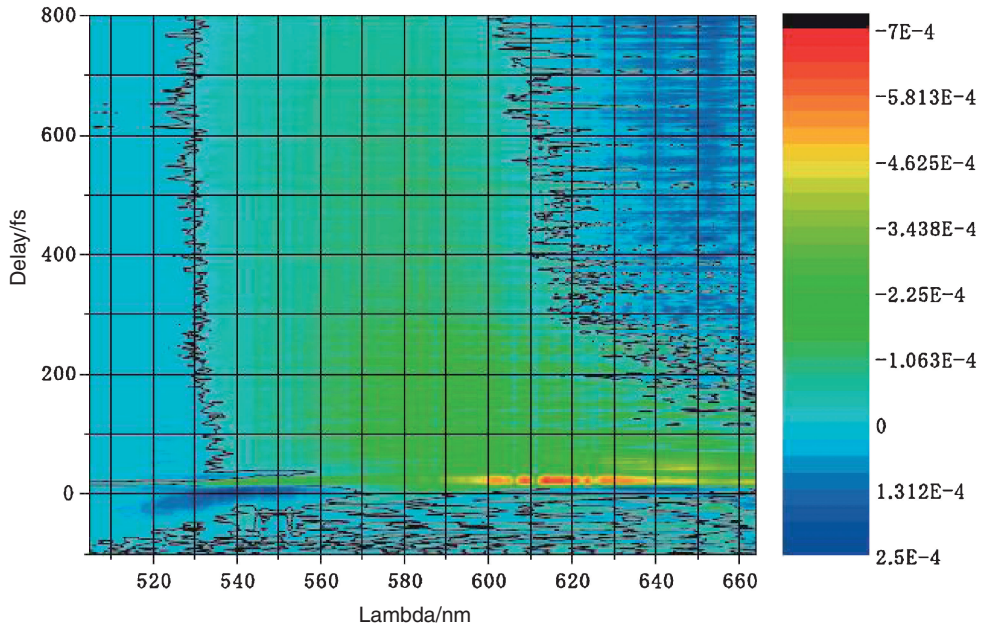

Figure 15. Two-dimensional display of probe wavelength–delay time transient absorption from the real-time traces probed at 128 different wavelengths.

The simultaneous measurement reduced systematic errors due to short- and long-term fluctuations in the laser intensity and also sample degradation, which is inevitable in experiments requiring long measurements.

Figure 14b shows the structural change of retinal chromophore during photoisomerization calculated by CIS/6-31G*// CIS/6-31G*. The structural changes in the retinal chromophore were calculated to obtain schematic views that depict the structural changes in retinyl chromophore in bR; however, the calculated structure may differ slightly from that of retinyl chromophore in bR, which is known to have a twisted conformation even in the K state.[73,74] The time constants for transitions from the ground state to the intermediate states I, J, and K determined from experimental results are consistent with the results obtained in studies by several groups including our group.[42,57,75] The probe wavelength dependence of the photoexcited dynamics was analyzed and it was found that the probe wavelength spectrum can be classified into four spectral regions based on the dynamics. This is because the electronic states have different effects on each spectral region. For the same reason, the dynamics of the molecular vibrational modes was also considered to be dependent on the probe wavelength. Herbst et al. found that the C=N stretching mode appears earlier than 500 fs after photoexcitation.[52] The present analysis of molecular vibrational modes reveals the existence of the C=N stretching mode, which decays within 30 fs after photoexcitation. This implies that the primary event immediately after photoexcitation is not the excitation of torsion around the C13=C14 bond, as has long been believed,[76] nor is it the C=C stretching mode, as was recently proposed.[49]

4.4 Spectrogram Analysis. The spectrograms (Figures 16a–16d) reveal the existence of a C=N stretching mode with a frequency of ca. 1640 cm^{-1}, whose vibration period is 20 fs. The C=N signal disappears after 30 fs. Because of the short lifetime of this mode, which corresponds to 1.5 oscillation periods, the Raman spectrum is expected to have a broad bandwidth of about 1100 cm^{-1}, which reduces the peak intensity by a factor of about 100 from that estimated from the Raman spectral width of the C=N mode in the ground state.[77] This makes it practically impossible to observe in the Raman spectrum. From the line width of the ground-state Raman signal of bR,[77] the decay time of the C=N stretching mode in the ground state is known to be slightly longer than 3 ps. The observed C=N signal decays much faster (<30 fs) than the appearance time (>200 fs) of the I state. Therefore, the observed Fourier signal of the C=N stretching frequency is thought not to be due to the G or I state. Rather, it is thought to be due to the H state, which is excited in the very initial stages of photoisomerization. The excited molecular vibration of the C=N stretching mode decays rapidly (<30 fs) in the H state, indicating that the C=N vibration oscillates less than two times. The H state then decays with a time constant of 235 ± 22 fs. This finding can explain the very interesting but controversial observation by Ruhman's group.[59] Even the locked retinal analogue can be deformed near the protonated C=N bond, resulting in spectral changes similar to those induced by isomerization. Therefore, the spectral changes commonly observed both in native retinal and artificial locked analogue are introduced by electronic changes near the protonated C=N bond, rather than the C13=C14 bond. After this conformational change near the C=N bond, the vibration of which is heavily damped, C=C stretching and torsion around the C13=C14 bond start.

Mathies' group[42] found that I state appears within about 200 fs. The positive ΔA about 200 fs after photoexcitation in the L_1 and L_2 spectral ranges indicates the contribution of the induced absorption due to the I state. In the probe spectral ranges, a new signal appears around 1800 cm^{-1} about 200 fs after excitation (Figures 8e and 8f), indicating that the signal is mainly due to the I state. This new mode is possibly related to highly distorted

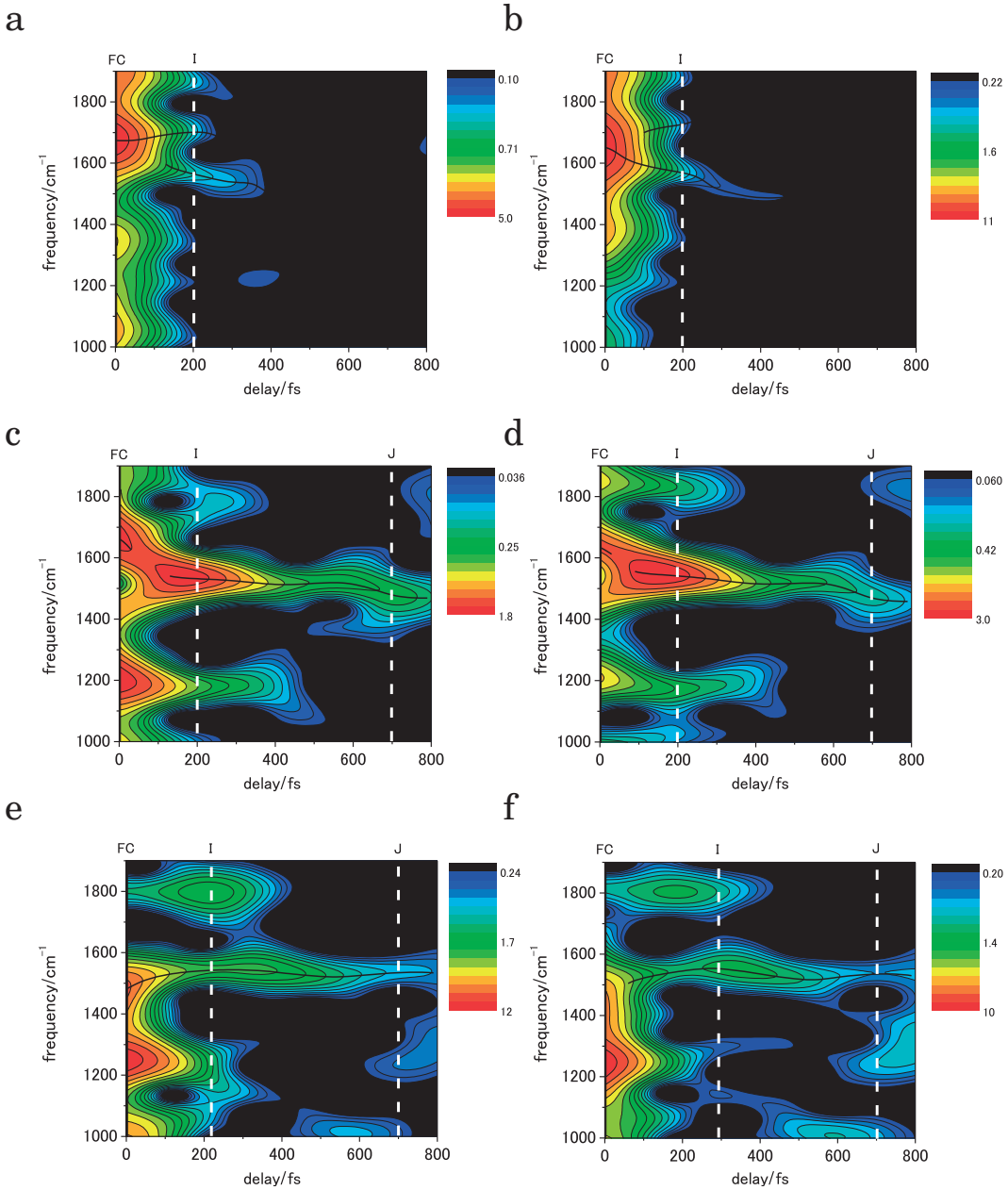

Figure 16. 3 Spectrograms calculated from the real-time traces measured at (a) 512, (b) 517, (c) 572, (d) 577, (e) 617, and (f) 622 nm. The white broken lines in the figures indicate the approximate appearance times of the H, I, and J states.

C=N stretching. The increase in the C=N stretching frequency to about 1800 cm^{-1} indicates that π-electron flow to the protonated Schiff base after the very rapid distortion partially neutralizes the positive charge of the N atom, increasing the bond order. This implies that the charge redistribution occurs from interaction with binding pocket residues and that the distortion relaxes on formation of the J intermediate.

4.5 Conclusion. Based on the results of the present study, it is concluded that the first process in the photophysical dynamics in bR is the deformation of the retinal configuration which decays within 30 fs near the C=N bond in the protonated Schiff base. It is followed by C=C stretching and then torsional motion of several periods around the C_{13}=C_{14} bond. This mode is as short as 30 fs, which corresponds to only 1.5 times the oscillation period (20 fs). This means that electronic redistribution, which occurs immediately after excitation (<2 fs), triggers rapid oscillation of C=N stretching. After a few oscillations, the energy is transferred to C=C stretching.

5. Summary and Future Prospects

In full analysis of the optical parametric processes we could obtain sub-5-fs pulse laser in visible to near infrared spectral range which is not only the world's shortest pulse source in the spectral range but also a useful reliable source for the study of ultrafast processes in molecules. Using the sub-5-fs pulse laser, we found various new phenomena, such as dynamic mode coupling between molecular vibrational modes, Duschinsky rotation, and a dynamic intensity borrowing effect.[78] During

photoisomerization of a biopolymer (bR), we directly observed instantaneous vibration spectrum deformed by the rotation in the retinal chromophore. Zewail et al. (Zewail won the Nobel Prize for Chemistry in 1999) performed time-resolved observations of the reactant and the product in a gas-phase reaction and pioneered transition state spectroscopy, but they were not able to observe spectra of transition states. We succeeded in observing vibrational spectra that reflect the molecular structure of transition states. We even applied this technique to a protein that has a complex molecular structure.

In ultrafast and broadband spectroscopy of bR, we found that the frequency of the C=C stretching mode was modulated along with the torsion motion around C_{13}=C_{14} during photoisomerization of bR. This reveals that the bond length of C_{13}=C_{14} is modulated on the deformation around C_{13}=C_{14} during photoisomerization.[70] A transition state during Raman-excited oxidation of chloroform was directly observed by ultrafast spectroscopy using broadband visible sub-5-fs pulses.[79] It has been demonstrated that the observation of transition states by sub-5-fs time-resolved spectroscopy is applicable for ground-state reactions as well as for excited-state reactions via Raman excitation in a wide variety of chemical reactions. Ultrafast spectroscopy was also used for direct observations of microstructural changes, which have been only predicted theoretically, like the initial structural change in photobiological processes such as photoisomerization in rhodopsin, bR,[80] and photodissociation of oxygen from oxyhemoglobin[81] as reviewed in this paper.

Development of ultrashort laser pulses meets many needs in various scientific fields as demonstrated by their wide variety of applications, including for defining frequency standards, for distance measurements, and for studying the ultrafast dynamics of chemicals, biological materials, and solid-state/condensed matter physics. Ultrashort laser pulses are also used in information technology and laser processing applications. In the present paper we described the usefulness of ultrashort pulse laser and ultrafast spectroscopy to understand chemical reactions. Using sub-5-fs pulse laser from NOPA, the transition state could be observed directly in the pump–probe type experiment utilizing the real-time observation of molecular vibration amplitudes through the modulation of transition probability by molecular vibration.

The author would like to acknowledge collaborators, Profs. A. Yabushita, A. Shirakawa, A. Baltuska, and Drs. Y. Wang, and Z. Wang for performing the research described in this article.

References

1 C.-K. Lee, J.-Y. Zhang, J. Huang, C.-L. Pan, *Opt. Express* **2003**, *11*, 1702.
2 P. Di Trapani, A. Andreoni, G. P. Banfi, C. Solcia, R. Danielius, A. Piskarskas, P. Foggi, M. Monguzzi, C. Sozzi, *Phys. Rev. A* **1995**, *51*, 3164.
3 V. Krylov, A. Kalintsev, A. Rebane, D. Erni, U. P. Wild, *Opt. Lett.* **1995**, *20*, 151.
4 S. R. Greenfield, M. R. Wasielewski, *Opt. Lett.* **1995**, *20*, 1394.
5 T. S. Sosnowski, P. B. Stephens, T. B. Norris, *Opt. Lett.* **1996**, *21*, 140.
6 R. Danielius, A. Piskarskas, P. Di Trapani, A. Andreoni, C. Solcia, P. Foggi, *Opt. Lett.* **1996**, *21*, 973.
7 J. Wang, M. H. Dunn, C. F. Rae, *Opt. Lett.* **1997**, *22*, 763.
8 T. Wilhelm, J. Piel, E. Riedle, *Opt. Lett.* **1997**, *22*, 1494.
9 G. Cerullo, M. Nisoli, S. De Silvestri, *Appl. Phys. Lett.* **1997**, *71*, 3616.
10 A. Shirakawa, T. Kobayashi, *Appl. Phys. Lett.* **1998**, *72*, 147.
11 M. Nisoli, S. Stagira, S. De Silvestri, O. Svelto, G. Valiulis, A. Varanavicius, *Opt. Lett.* **1998**, *23*, 630.
12 G. Cerullo, M. Nisoli, S. Stagira, S. De Silvestri, *Opt. Lett.* **1998**, *23*, 1283.
13 A. Shirakawa, I. Sakane, T. Kobayashi, *Opt. Lett.* **1998**, *23*, 1292.
14 A. Shirakawa, I. Sakane, M. Takasaka, T. Kobayashi, *Appl. Phys. Lett.* **1999**, *74*, 2268.
15 G. Cerullo, M. Nisoli, S. Stagira, S. De Silvestri, G. Tempea, F. Krausz, K. Ferencz, *Opt. Lett.* **1999**, *24*, 1529.
16 D. Zeidler, T. Hornung, D. Proch, M. Motzkus, *Appl. Phys. B* **2000**, *70*, S125.
17 T. Kobayashi, A. Shirakawa, *Appl. Phys. B* **2000**, *70*, S239.
18 E. Riedle, M. Beutter, S. Lochbrunner, J. Piel, S. Schenkl, S. Spörlein, W. Zinth, *Appl. Phys. B* **2000**, *71*, 457.
19 J. Piel, M. Beuter, E. Riedle, *Opt. Lett.* **2000**, *25*, 180.
20 M. R. Armstrong, P. Plachta, E. A. Ponomarev, R. J. D. Miller, *Opt. Lett.* **2001**, *26*, 1152.
21 M. Zavelani-Rossi, G. Cerullio, S. De Silvestri, L. Gallmann, N. Matuschek, G. Steinmeyer, U. Keller, G. Angelow, V. Scheuer, T. Tschudi, *Opt. Lett.* **2001**, *26*, 1155.
22 M. Zavelani-Rossi, D. Polli, G. Cerullo, S. De Silvestri, L. Gallmann, G. Steinmeyer, U. Keller, *Appl. Phys. B* **2002**, *74*, s245.
23 A. Baltuška, T. Fuji, T. Kobayashi, *Opt. Lett.* **2002**, *27*, 306.
24 A. Baltuška, T. Fuji, T. Kobayashi, *Opt. Lett.* **2002**, *27*, 1241.
25 G. Cirmi, D. Brida, C. Manzoni, M. Marangoni, S. De Silvestri, G. Cerullo, *Opt. Lett.* **2007**, *32*, 2396.
26 D. Brida, M. Marangoni, C. Manzoni, S. De Silvestri, G. Cerullo, *Opt. Lett.* **2008**, *33*, 2901.
27 M. Ghotbi, M. Beutler, V. Petrov, A. Gaydardzhiev, F. Noack, *Opt. Lett.* **2009**, *34*, 689.
28 R. Danielius, A. Piskarskas, A. Stabinis, G. P. Banfi, P. Di Trapani, R. Righini, *J. Opt. Soc. Am. B* **1993**, *10*, 2222.
29 C. Chen, B. Wu, G. You, A. Jiang, *Sci. Sin., Ser. B* **1985**, *28*, 235.
30 C. Chen, Y. X. Fan, R. C. Eckardt, R. L. Byer, *SPIE Proc.* **1986**, *681*, 12.
31 W. R. Bosenberg, L. K. Cheng, C. L. Tang, *Appl. Phys. Lett.* **1989**, *54*, 13.
32 D. Eimerl, L. Davis, S. Velsko, E. K. Graham, A. Zalkin, *J. Appl. Phys.* **1987**, *62*, 1968.
33 T. G. Giallorenzi, C. L. Tang, *Phys. Rev.* **1968**, *166*, 225.
34 D. A. Kleinman, *Phys. Rev.* **1968**, *174*, 1027.
35 L. Tang, in *Quantum Electronics: A Treatise*, ed. by H. Rabin, C. L. Tang, Academic, IA, New York, **1975**.
36 R. L. Byer, R. L. Herbst, in *Nonlinear Infrared Generation*, ed. by Y. R. Shen, Springer-Verlag, New York, **1977**, Vol. 96.
37 P. Di Trapani, A. Andreoni, C. Solcia, P. Foggi, R. Danielius, A. Dubietis, A. Piskarskas, *J. Opt. Soc. Am. B* **1995**, *12*, 2237.
38 Zs. Bor, B. Rácz, *Opt. Commun.* **1985**, *54*, 165.
39 O. E. Martinez, *Opt. Commun.* **1986**, *59*, 229.

40 R. Zhang, D. Pang, J. Sun, Q. Wang, S. Zhang, G. Wen, *Opt. Laser Technol.* **1999**, *31*, 373.
41 R. Danielius, A. Piskarskas, P. Di Trapani, A. Andreoni, C. Solcia, P. Foggi, *IEEE J. Quantum Electron.* **1998**, *34*, 459.
42 W. T. Pollard, C. H. B. Cruz, C. V. Shank, R. A. Mathies, *J. Chem. Phys.* **1989**, *90*, 199.
43 Y. Shichida, T. Yoshizawa, T. Kobayashi, H. Ohtani, S. Nagakura, *FEBS Lett.* **1977**, *80*, 214.
44 Y. Shichida, T. Kobayashi, H. Ohtani, T. Yoshizawa, S. Nagakura, *Photochem. Photobiol.* **1978**, *27*, 335.
45 K. Suzuki, T. Kobayashi, H. Ohtani, H. Yesaka, S. Nagakura, Y. Shichida, T. Yoshizawa, *Photochem. Photobiol.* **1980**, *32*, 809.
46 D. Oesterhelt, W. Stoeckenius, *Methods of Enzymology, Biomembranes Part A*, Academic Press, New York, **1995**, Vol. 31.
47 Y. Huang, S.-T. Wu, Y. Zhao, *Opt. Express* **2004**, *12*, 895.
48 A. P. Shreve, R. A. Mathies, *J. Phys. Chem.* **1995**, *99*, 7285.
49 R. González-Luque, M. Garavelli, F. Bernardi, M. Merchán, M. A. Robb, M. Olivucci, *Proc. Natl. Acad. Sci. U.S.A.* **2000**, *97*, 9379.
50 W. Humphrey, H. Lu, I. Logounov, H.-J. Werner, K. Schulten, *Biophys. J.* **1998**, *75*, 1689.
51 S. Schenkl, F. van Mourik, G. van der Zwan, S. Haacke, M. Chergui, *Science* **2005**, *309*, 917.
52 J. Herbst, K. Heyne, R. Diller, *Science* **2002**, *297*, 822.
53 G. Haran, K. Wynne, A. Xie, Q. He, M. Chance, R. M. Hochstrasser, *Chem. Phys. Lett.* **1996**, *261*, 389.
54 F. Gai, K. C. Hasson, J. C. McDonald, P. A. Anfinrud, *Science* **1998**, *279*, 1886.
55 J. A. Stuart, D. L. Marcy, K. J. Wise, R. R. Birge, *Synth. Met.* **2002**, *127*, 3.
56 L. Song, M. A. El-Sayed, *J. Am. Chem. Soc.* **1998**, *120*, 8889.
57 M. Du, G. R. Fleming, *Biophys. Chem.* **1993**, *48*, 101.
58 A. Kahan, O. Nahmias, N. Friedman, M. Sheves, S. Ruhman, *J. Am. Chem. Soc.* **2007**, *129*, 537.
59 B. Hou, N. Friedman, M. Ottolenghi, M. Sheves, S. Ruhman, *Chem. Phys. Lett.* **2003**, *381*, 549.
60 A. C. Terentis, Y. Zhou, G. H. Atkinson, L. Ujj, *J. Phys. Chem. A* **2003**, *107*, 10787.
61 M. Olivucci, A. Lami, F. Santoro, *Angew. Chem., Int. Ed.* **2005**, *44*, 5118.
62 S. Hayashi, E. Tajkhorshid, K. Schulten, *Biophys. J.* **2003**, *85*, 1440.
63 X. Chen, V. S. Batista, *J. Photochem. Photobiol., A* **2007**, *190*, 274.
64 O. Weingart, *J. Am. Chem. Soc.* **2007**, *129*, 10618.
65 T. S. Rose, M. J. Rosker, A. H. Zewail, *J. Chem. Phys.* **1988**, *88*, 6672.
66 J. C. Polanyi, A. H. Zewail, *Acc. Chem. Res.* **1995**, *28*, 119.
67 F. Schotte, J. Soman, J. S. Olson, M. Wulff, P. A. Anfinrud, *J. Struct. Biol.* **2004**, *147*, 235.
68 B. J. Siwick, J. R. Dwyer, R. E. Jordan, R. J. D. Miller, *Science* **2003**, *302*, 1382.
69 R. Srinivasan, J. S. Feenstra, S. T. Park, S. Xu, A. H. Zewail, *Science* **2005**, *307*, 558.
70 T. Kobayashi, T. Saito, H. Ohtani, *Nature* **2001**, *414*, 531.
71 D. W. McCamant, P. Kukura, R. A. Mathies, *Appl. Spectrosc.* **2003**, *57*, 1317.
72 T. Kobayashi, Z. Wang, *New J. Phys.* **2008**, *10*, 065015.
73 B. Schobert, J. Cupp-Vickery, V. Hornak, S. O. Smith, J. K. Lanyi, *J. Mol. Biol.* **2002**, *321*, 715.
74 Y. Matsui, K. Sakai, M. Murakami, Y. Shiro, S.-i. Adachi, H. Okumura, T. Kouyama, *J. Mol. Biol.* **2002**, *324*, 469.
75 M. Taiji, K. Bryl, M. Nakagawa, M. Tsuda, T. Kobayashi, *Photochem. Photobiol.* **1992**, *56*, 1003.
76 J. Dobler, W. Zinth, K. Kaiser, D. Oesterhelt, *Chem. Phys. Lett.* **1988**, *144*, 215.
77 K. C. Hasson, F. Gai, P. A. Anfinrud, *Proc. Natl. Acad. Sci. U.S.A.* **1996**, *93*, 15124.
78 H. Kano, T. Kobayashi, *J. Chem. Phys.* **2002**, *116*, 184.
79 I. Iwakura, A. Yabushita, T. Kobayashi, *Chem. Phys. Lett.* **2008**, *457*, 421.
80 A. Yabushita, T. Kobayashi, *Biophys. J.* **2009**, *96*, 1447.
81 T. Kobayashi, A. Yabushita, *Chem. Phys. Lett.* **2009**, *482*, 143.

Takayoshi Kobayashi was born in Japan in 1944. He received his B.Sc. (1967), M.Sc. (1968), and Ph.D. (1972) degrees from the University of Tokyo. He was a senior research assistant in Institute of Physical and Chemical Research (RIKEN) from 1972 to 1980 and also an invited temporary member of the technical staff in Bell Laboratory in USA from 1977 to 1979. He became an associate professor of the University of Tokyo in 1980 and a full professor in 1994. He moved to the University of Electro-Communications as a specially appointed professor from 2006. His main research areas are ultrashort pulse laser/ultrafast processes, molecular physics, and quantum electronics/quantum information. He received Scientific Achievement Award from the Chemical Society of Japan (1995), Scientific Achievement Award from the Spectroscopy Society of Japan (2003), Scientific Achievement Award from the Matsuo Foundation (2005), Outstanding Visiting Professor of Chinese Academy of Science, Institute of Physics in Beijing (2010), Outstanding Contribution to Science and Technology Award from the Shimadzu Science and Technology Foundation (2010), Japan Minister of Education, Culture, Sports, Science and Technology Award for Outstanding Contribution to Science and Technology (2010), Humboldt Award for Outstanding Research in the Development of Ultrashort Pulse Laser and Ultrafast Processes in Molecules (2011), The Chemical Society of Japan Award for Outstanding Research in the Development of Ultrashort Pulse Laser and Ultrafast Chemical Processes in Molecules (2011). Outstanding Visiting Professor of Chinese Academy of Science, Shanghai Institute of Optic's and Fine Mechanics in Shanghai (2011).